This is a peer-reviewed, accepted author manuscript of the following research article: Júnior, AFG, Azzolin, CP, Castillo, CAR & Carneiro, VGA 2022, 'Availability analysis of a ship-to-ground FSO link', Journal of Optical Communications and Networking, vol. 14, no. 5, pp. 339-350. https://doi.org/10.1364/JOCN.439148

Availability Analysis of a Ship-to-Ground FSO Link

AIRTON F. G. JÚNIOR[1], CLAISSO P. AZZOLIN[1], CLAUDIO A. R. CASTILLO[2], AND VÍTOR G. A. CARNEIRO[1]

[1] Department of Defense Engineering, Military Institute of Engineering, Rio de Janeiro, RJ
[2] Federal University of Rio de Janeiro, Rio de Janeiro, RJ, Brazil
[*] Corresponding author: andrezo@ime.eb.br

Compiled December 28, 2021

This article analyzes the availability of a Free-Space Optical (FSO) communication link, established between a maritime platform and a land base. In this analysis, the impact of the laser beam misalignment, caused by the vessel's six oscillatory motions in a seaway, is considered. The hydrodynamic system is modeled, through a ship's Response Amplitude Operator (RAO), under a typical sea state condition. Finally, the link availability is calculated, based on FSO losses, considering a beam with Gaussian power distribution.

http://dx.doi.org/10.1364/ao.XX.XXXXXX

1. INTRODUCTION

In the context of mobile communications, either military or civilian, free-space optical (FSO) links present some potential advantages over radio frequency communications [1]. Due to its high bandwidth, it is possible to transmit a significantly greater amount of information, by means of an extremely directional optical beam, thus hindering the possibility of detection and intentional interference in the transmitted signal [2]. FSO systems are easily deployable and can be reinstalled without the cost of a dedicated fiber-optic cable. They are also capable of satisfying even the most demanding throughput requirements of today's high definition television (HDTV) broadcasting applications [3].

Despite these advantages, the propagation of optical waves in free space is highly susceptible to atmospheric effects, such as absorption and spreading by molecules and aerosols, especially during rain or fog [4]. In addition, atmospheric turbulence has a strong impact on the availability of FSO links, generating effects such as scintillation, beam wander, and beam spreading [5]. Many studies have been carried out to reduce the effects cited above, as well as enabling the implementation of FSO on mobile platforms. In this context, the Naval Research Laboratory (NRL) conducted a high-availability communications test, during a military exercise, in the regions of San Diego and Honolulu, where FSO links were established between US Navy ships [6, 7]. Other studies have been developed aiming to make possible the use of FSO systems in high-speed trains (HST) [8–11].

One of the main concerns in all of these studies is pointing, acquisition and tracking (PAT), which represents a great challenge for the consolidation of these communication systems [12]. Pointing errors can arise from vibrations of the equipment base, motions of mobile platforms, failures in the tracking system, or boresight errors, which are fixed displacements between beam and receiver centers [13, 14]. Hence, they can degrade the availability of the system and even interrupt the link [15, 16].

The availability of terrestrial FSO links is a subject that has been heavily studied. In [17], an assessment of the availability rate of FSO and FSO/RF hybrid systems was carried out, considering the effects of atmospheric attenuation, and in [18], losses caused by the phenomenon of atmospheric turbulence were considered, modeled based on the theory of Rytov's scintillation. In [19], an estimate was made of the availability of FSO links, based on attenuations caused by fog, and in [20], the authors considered the impacts caused by rain in a country with a tropical climate. This performance parameter was also analyzed on other platforms, such as an airborne link, but considering the influences of losses caused by a generalized misalignment [21].

The use of FSO in vessels brings great challenges. Even if the vessel is anchored, the forces and moments of ocean waves cause translational and angular deviations in the transmitted optical beam. The setting proposed in this article is the following: an FSO transceiver (TX) is installed on a ship, which is anchored at a position close to the coast; meanwhile, the receiver (RX) is fixed in a mast positioned on the beach (see Fig 1). Due to its placement, TX is under the influence of the motions, caused by the interaction of the ship with the ocean waves. It is also considered that the bow of the ship is, on average, pointed towards the beach in a position perpendicular to the coast.

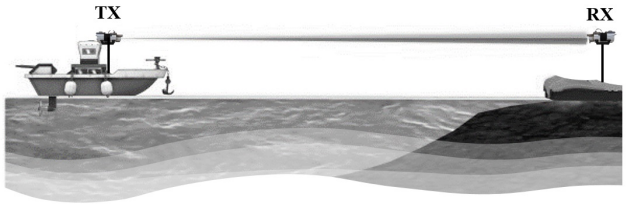

Fig. 1. Maritime FSO communication link.

Taking this scenario into consideration, this study analyzes the influence of the ship's wave-induced motions on the behavior of the communications system. In this sense, geometric, atmospheric, scintillation, and misalignment losses are calculated, considering that the optical beam is circular with Gaussian power distribution. Hence, this article aims to analyze the availability of a maritime FSO communication link, considering the influence of the ship's translational and angular motions.

To this purpose, Section II shows some aspects related to the system modeling. Both hydrodynamic and FSO subsystems are presented in this section. The results are discussed in Section III. Finally, the conclusions are presented in Section IV.

2. SYSTEM MODELING

For the sake of simplicity, the present study was divided into two main subsystems: hydrodynamic and optical. The flowchart of Fig. 2 shows the steps involved in modeling the two problems.

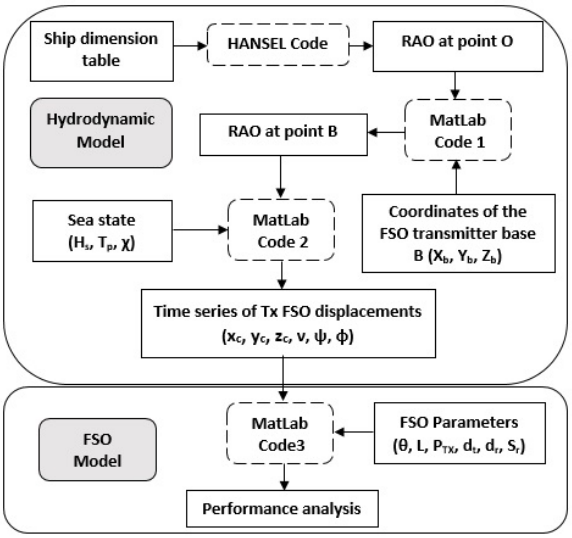

Fig. 2. Flowchart with the steps involved in modeling the maritime FSO communication link.

In general, the solution to the hydrodynamic problem consists of calculating the motions of the ship that influence the alignment of the FSO link. In this modeling, the hydrodynamic subsystem receives, as input, the parameters of a given sea state and provides, as output, the time series of motions that act at the base of the FSO transmitter. The transfer functions that establish a relationship between the inputs and outputs of this system are known as Response Amplitude Operator (RAO). The ship's RAO curves have a direct influence on the availability of the optical communication system.

The behavior of the sea is characterized by three parameters: H_s, T_p and χ. The FSO subsystem is described by the parameters θ, L, P_{Tx}, d_t, d_r and S_r. The performance analysis is based on the availability of the optical link. The meaning of these variables will be introduced in the next subsections.

A. Hydrodynamic Subsystem

A.1. Input parameters

As previously said, the hydrodynamic model receives three parameters that describe the behavior of the sea in the ship's anchoring position. This description uses statistical parameters, such as significant wave height (H_s) and peak period (T_p) of the sea spectrum. H_s is the average wave height of the highest one-third of the waves, taken from a time series record of a given sea state, while T_p is the period of maximum energy, observed in the sea spectrum [22–24].

Based on these definitions, it is possible to evaluate, through the wave scatter diagram, the occurrence probability of a given sea state for a specific ocean region. This diagram relates the number of occurrences of the pairs (H_s, T_p) to the total number of ocean waves, observed for several years in the geographic region of interest. Table 1 shows the annual mean wave scatter diagram for area 11-32 (southeast coast of Brazil), averaged over 10 years of numerical weather prediction, by the National Maritime Research Institute [25]. In Tab. 1, class intervals of H_s and T_p have been defined to count the occurrences. In order to specify one single value to represent each interval, the middle point within each range was used.

Table 1. Wave Scatter Diagram for the Southeast Coast of Brazil

H_s (m)	T_p (s)							TOTAL
	2 - 4	4 - 6	6 - 8	8 - 10	10 - 12	12 - 14	14 - 16	
7.5 - 8.0					0.00034			0.00034
7.0 - 7.5					0.00159	0.00007		0.00166
6.5 - 7.0					0.00166	0.00112		0.00278
6.0 - 6.5				0.00224	0.00621	0.00790		0.01635
5.5 - 6.0				0.01194	0.01387	0.02367	0.00027	0.04975
5.0 - 5.5			0.00024	0.03815	0.03812	0.05796	0.00217	0.13664
4.5 - 5.0			0.00465	0.08608	0.12399	0.10307	0.00648	0.32427
4.0 - 4.5			0.04158	0.23330	0.27094	0.19877	0.02486	0.76945
3.5 - 4.0			0.27556	0.43631	0.53609	0.41854	0.07214	1.73864
3.0 - 3.5		0.00020	1.08320	0.99051	1.06234	0.87540	0.12755	4.13920
2.5 - 3.0		0.01648	3.26143	2.21920	2.22171	1.74653	0.17707	9.64242
2.0 - 2.5		0.12999	6.51361	4.64552	4.86349	2.43795	0.14529	18.7359
1.5 - 2.0	0.00070	0.86601	9.01983	9.94359	6.97481	2.59206	0.10520	29.5022
1.0 - 1.5	0.00020	0.95463	7.32552	12.2426	5.35464	1.63160	0.06451	27.5737
0.5 - 1.0	0.00265	0.17910	2.10694	2.77194	0.97437	0.30666	0.00672	6.34838
0.0 - 0.5	0.86421	0.01184	0.04077	0.05738	0.03415	0.01038	0.00027	1.01900
TOTAL	0.86776	2.15825	29.6733	33.67876	22.4783	10.4117	0.73253	100.000

Thus, the representative values of pairs, which were called (H_{srp}, T_{prp}), were used, as input parameters, for the mathematical description of the sea behavior in the region where the ship operates. This mathematical description, also known as JONSWAP spectrum [26], is commonly used in the analyses of ocean systems operating on the coast [27, 28].

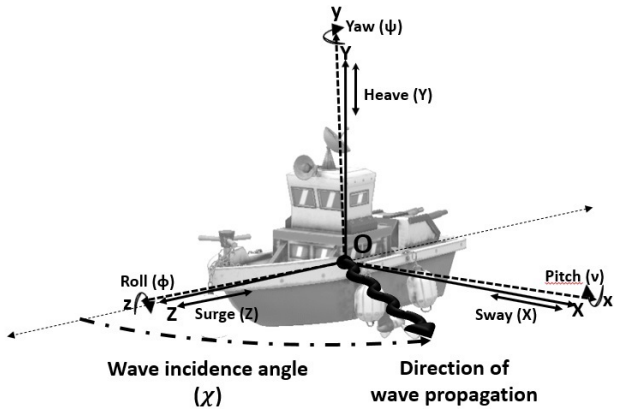

Fig. 3. Definition of the ship's motions and wave incidence angle.

The wave incidence angle (χ), illustrated in Fig. 3, is another important parameter, used to define the ship's behavior at sea. It characterizes the main direction of wave propagation, relative to the ship heading, and its value is equal to the opening angle, measured counterclockwise from the ship's bow [29].

In this study, it was considered the influence of four wave incidence angles (0°, 90°, 135° and 180°), which affect the vessel's hull. Since the bow of the ship is, on average, pointing to the beach, the incidence of $\chi = 0°$ (stern sea) will predominate.

A.2. Ship Transfer Functions

The ship used in this study is the US Navy Ship (USNS) American Mariner, which was commissioned by the North American Armed Forces. Its main characteristics are summarized in Table 2. This ship was chosen, due to its military characteristics and open access to information related to its hull geometry [30].

Table 2. Main Characteristics of the MARINER Ship

Parameter	Description	Value
L_s	Length	160.9m
W	Beam (width)	23.1m
D	Draft	9.068m

The output variables of the hydrodynamic subsystem were obtained by analyzing the sea influence on the ship. When the ocean waves encounter the ship's hull, the vessel develops translational motions along the X, Y and Z axes, called sway, heave and surge, respectively. Besides, angular motions are also observed, around the axes of the body (x, y, z), defined as pitch, yaw and roll (υ, ψ, ϕ), as represented in Fig. 3 [31]. It should be noted that the notation adopted for the axes follows the optical typical nomenclature, instead of the traditional hydrodynamics nomenclature, for the sake of compliance between the different areas of study.

In the classic study of the ship's behavior at sea, the floating body develops linear and harmonic motions relative to a point, whose average position is adopted as the origin of an inertial reference system [32]. When the ship is anchored, the forward speed is zero ($U = 0$). Hence, this inertial system is fixed in space and coincides with the ship's average position. The origin of this system (point O) is a Newtonian reference, whose longitudinal position (ZG), for the American Mariner, is located at 83.39 m after the ship's Forward Perpendicular (F.P.), as shown in Fig. 4. The vertical position (YG) is on the line that indicates the ship's load waterline length (LWL), just 90.5 cm above the vessel's Center of Gravity (G). The transverse position coincides with its centerline (diametrical plane), i.e., $XG = 0$ m.

In this study, the HANSEL program was used to calculate the RAO values for the six motions and the four previously defined wave incidence angles [30]. HANSEL is a computational tool, based on linear potential theory in frequency domain, used in seakeeping analysis. This program requires the vessel's underwater geometry to be input as offset points for several cross sections along the ship. The RAO values are associated with the inherent characteristics of the ship for a given loading condition, excitation period, and incidence angle, i.e., they represent the responses (amplitudes and phases) of the floating system to regular waves. Based on these parameters and the knowledge of the characteristics of the sea state, it is possible to determine

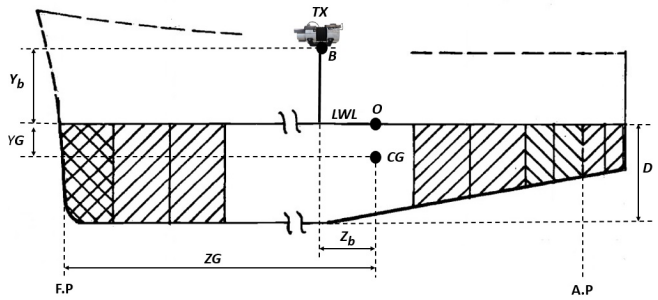

Fig. 4. Definition of the O point reference system.

the displacements, speeds, and accelerations at any point of the ship's hull. The RAO is defined as [29]:

$$\mathrm{RAO}_i(\omega_e, \chi) = \frac{S_{ia}}{\zeta_a} \quad \textbf{(1)}$$

where S_{ia} is the response amplitude of the i-th degree of freedom and ζ_a is the amplitude of the regular wave in meters. The amplitudes of the translational motions ($i = 1, 2, 3$) are given in meters and those of the rotational motions ($i = 4, 5, 6$) are in degrees. ω_e is the encounter frequency, defined as the frequency at which the ship encounters the waves of frequency ω_w [24]. In this work, since $U = 0$, $\omega_e = \omega_w$.

Since Hansel's output provides the responses at the ship's origin O, the translational motions at a generic point of the ship are obtained by a transformation of reference axes [24]. The rotational motions are always the same, independently of which point in being considered. In this way, it is possible to calculate the RAO values of the FSO TX absolute displacements, installed at point B (x_b = 0 m, y_b = 20 m, z_b = 10 m).

A.3. Output Parameters

The response of a ship, under real sea conditions, can be determined by the linear superposition of each regular wave component that is used to model the real sea [33]. Hence, the motions in irregular waves, are obtained by adding regular waves of different amplitudes, frequencies, and directions of propagation. Based on the wave energy spectrum and the frequency characteristics of the ship's RAOs, the response spectrum and statistics can be found [33]. The response spectrum, $S_{ia}(\omega_e)$, is obtained through [29]:

$$S_{ia}(\omega_e) = S_\varepsilon(\omega_e)[RAO_i(\omega_e, \chi)]^2, \quad \textbf{(2)}$$

where $S_\varepsilon(\omega_e)$ is the sea spectrum.

The proposed FSO system was simulated, positioned on the maritime platform presented in Fig. 4. The RAO values produced by HANSEL, were used in MatLab Code 1 (see Fig. 2) to calculate the RAO spectrum at point B. This spectrum and the information related to the sea state (Hs, Tp, χ) were, subsequently, inserted into MatLab Code 2, which implements Eq. 2 to obtain the Mariner's response spectrum, given the desired sea conditions.

Finally, in order to obtain the time series of the ship's motions at the point of interest (FSO TX), this second code used the MatLab´s WAFO toolbox [34], to generate temporal records from the ship response spectrum. This way, the time series for the six degrees of freedom were calculated for a time window of 20 minutes.

B. Optical Subsystem

The time series of the motions at the FSO TX were used as input parameters to the optical subsystem. The availability of the FSO link was analyzed, considering a laser with Gaussian power distribution as optical source. A Gaussian beam is a natural by-product of the laser forming process in a resonant cavity [35]. For this reason, lasers used in optical communications operate, many times, in the fundamental transverse electromagnetic mode (TEM_{00}), which produces a Gaussian profile [36]. The optical intensity can be observed through the irradiance profile, given in cylindrical coordinates by [37]:

$$I(\rho, \phi, z) = I_0^2 \frac{r_t^2}{r_L^2(z)} \exp\left[-\frac{2\rho^2}{r_L^2(z)}\right], \quad (3)$$

where I_0 is a constant related to power at the TX output, $r_L(z) = r_t + \frac{\theta \cdot z}{2}$ is the beam width along z, r_t is the TX scope radius and θ is the beam divergence angle.

The detected power is obtained by the integration of the irradiation profile over the surface of the receiver. In order to include the effects of radial misalignment, it is necessary to translate axes over Eq. (3). Using rectangular coordinates, the peak of the Gaussian beam can be translated by x_c and y_c away from the origin, representing translational motions of TX, while the center of RX remains on the origin. Hence, the power of the misaligned beam, at the receiver ($Z = L$), is given by [38]:

$$P_{RX} = \int_S I_0^2 \frac{r_t^2}{r_L^2} \exp\left[-\frac{2[(x-x_c)^2 + (y-y_c)^2]}{r_L^2}\right] dS, \quad (4)$$

where S is the aperture area of the receiver.

Due to its availability gain in simulations of misaligned links, especially in moving systems, a recently proposed formulation was used to the combined geometric and radial misalignment attenuation, which is given, in dB, by [38]:

$$\alpha_{gm}[dB] = 10 \cdot \log_{10}\left[1 - Q_1\left(\frac{2d}{r_L}, \frac{2r_r}{r_L}\right)\right], \quad (5)$$

where Q_1 is the Marcum Q-function of order 1, d is the absolute radial misalignment and r_r is the RX aperture radius.

Eq. (5) can also be used to include angular misalignment between TX and RX, i.e., rotational motions. This way, α_{gm} can be calculated approximating d by

$$d = \sqrt{[x_c + L \cdot \tan(\phi)]^2 + [y_c + L \cdot \tan(\upsilon)]^2}, \quad (6)$$

where ϕ represents the yaw, υ the pitch angle of rotation and L the link distance. Regarding the other two motions, z_c was included as variations in L and ψ was considered when making the hydrodynamic calculations of x_c and y_c.

Beside geometric and misalignment losses, scintillation was also considered. This effect is caused by refractive index irregularities and, for its complete study, a statistical approach is necessary. However, some authors developed an attenuation coefficient due to scintillation, bringing a deterministic simplification to this statistical effect [5, 39, 40]. For this work, the effect of misalignment is considered to have a greater impact on the availability of the link than scintillation. Hence, a simplified model was used, based on Andrews's method [40].

Scintillation is usually described by the structural parameter of the refractive index, C_n^2, which represents the impact of the turbulence on the oscillation of optical power [5]. The parameter C_n^2 can range from 10^{-15} to 10^{-12} $m^{-2/3}$, which are characteristic values for weak and strong turbulences, respectively. In this work, $C_n^2 = 10^{-14}$ $m^{-2/3}$ was chosen, which corresponds to a scintillation loss between 1 and 1.56 dB for the distances considered in the scenario of Fig.1 [41].

Atmospheric attenuation is caused by the absorption and spreading of the light in the atmosphere components [42]. The proposed FSO system was designed to operate under conditions of clean weather and fine fog. This corresponds to an operational range of α_{atm} between 1 dB/km and 2 dB/km.

Thus, the total loss on the FSO maritime link is, in dB [43]:

$$\alpha_{tot}[dB] = \alpha_{gm} + \alpha_{atm}.L + \alpha_{scint} + \alpha_T + \alpha_R, \quad (7)$$

where α_{scint} is the loss due to scintillation, and α_T and α_R are the losses in the fiber-telescope interfaces of the transmitter and receiver, respectively. All losses are given in dB.

C. Availability Analysis

Simulations were carried out to evaluate the influence of ship motions upon the availability of the FSO system. These analyses were developed, based on the observation of the received power over time. This way, the system availability rate (η) was calculated. In communications, the availability is usually expressed as a percentage of uptime in one year. Nevertheless, due to the periodical characteristic of maritime waves, a sequence of uptimes and downtimes is observed in a time scale of minutes, depending on the sea state.

Thus, the availability rate was obtained through the relation between uptime (t_{up}) and total simulation time (t_T), i.e.,

$$\eta = t_{up}/t_T = t(d < d_{max})/t_T, \quad (8)$$

where t_{up} is the time in which the received power (P_{RX}) remains above the sensitivity level of the receiver (S_r).

This rate can also be expressed by analyzing the behavior of the total link misalignment over time. In this context, we define d_{max} as the maximum admitted misalignment at which the power reaches the threshold ($P_{RX} = S_R$). Thus, the availability rate is also given by the second part of Eq. 8.

3. SIMULATION, RESULTS AND DISCUSSION

A. Simulations of the Hydrodynamic Subsystem

During the seakeeping analysis in frequency-domain, sixty regular wave frequencies were considered. These frequencies correspond to the range of 2 s $< T <$ 28 s and were defined in a configuration file of input parameters in HANSEL. This data file was processed by HANSEL, to obtain the values of the amplitudes and phases of the ship's motions for the four different wave incidence angles. Based on these values, the Mariner's RAO curves at point O were obtained. Fig. 5 shows the RAO amplitudes for $\chi = 0°, 90°, 135°, 180°$.

The maximum amplitude of the translational motions (1.514 m/m) is observed for the heave motion at T = 7.748 s, when $\chi = 90°$. For the rotational motions, the maximum amplitude (9.187°/m) is observed for roll at T = 13 s, when $\chi = 90°$. However, due to the FSO longitudinal transmission axis, pitch and yaw motions cause a higher impact, especially in their resonance points. This will be noted when the availability results are presented, as a low availability at T = 11 s. Fig. 5 also shows that the pitch motion produces two main resonances: 1.256°/m, for (T = 11.51 s, $\chi = 180°$); and 1.514°/m, for (T = 7.747 s, $\chi = 135°$). The yaw maximum value is 0.588°/m, for (T = 12.49 s, $\chi = 135°$).

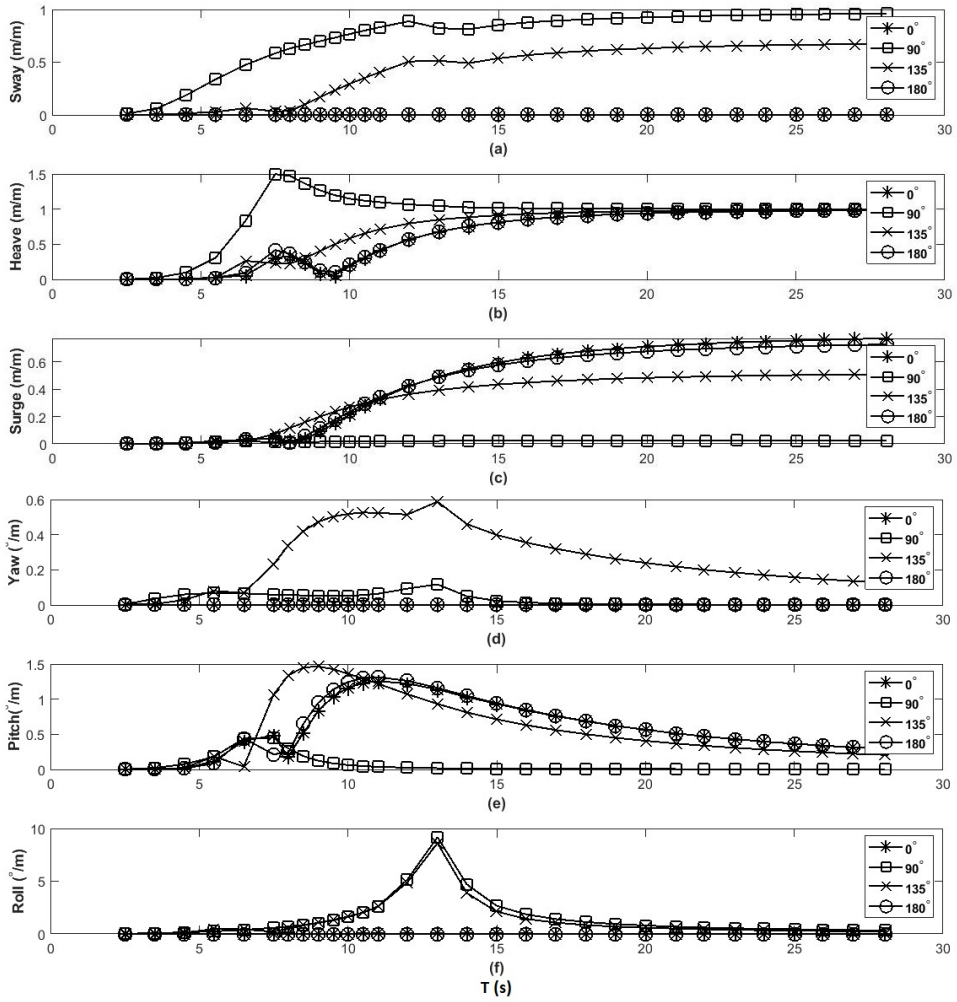

Fig. 5. RAO curves for the six motions at point O: (a) Sway, (b) Heave, (c) Surge, (d) Yaw, (e) Pitch, and (f) Roll.

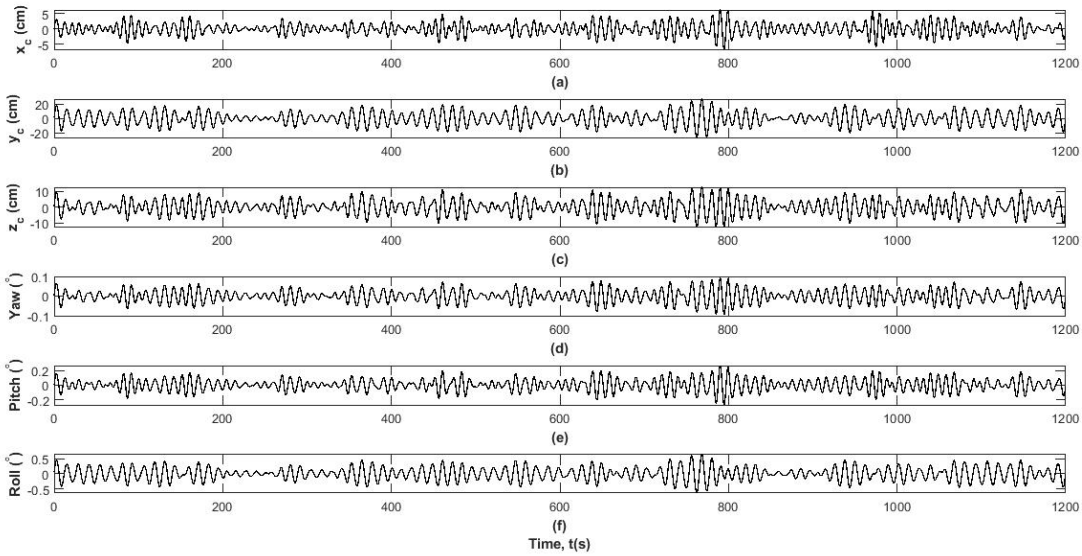

Fig. 6. Time series of FSO TX displacements for the sea state (H_s = 0.25 m, T_p = 11 s, $\chi = 135°$).

The values of amplitude presented in Fig. 5 were used in MatLab Code 1 (see Fig. 2) to calculate the RAO at point B. With this data and the sea spectrum, MatLab Code 2 was used to calculate the motions that act at the base of the FSO TX, which are shown in the time series of Fig. 6. The sea state (H_s = 0.25 m, T_p = 11 s, $\chi = 135°$) was chosen to evaluate the impact of the yaw and pitch motions, when the ship is in a resonant condition. This figure shows that the greater motions occurred for Y_p (heave) and roll motions.

Following the flowchart of Fig. 2, MatLab Code 3 was used to obtain the optical availability for the four incidence angles and all pairs of representative values (H_s, T_p) of the scatter diagram (Tab. 1). However, due to conciseness, we chose to show only the results for the sea state (H_s = 0.25 m, T_p = 11 s) and $\chi = 135°$, angle at which the vessel develops motions in all six degrees of freedom. The next subsection presents the optical results, used to obtain the availability. Whenever a time-domain analysis is shown, this resonant state was chosen.

B. Simulations of the Optical Subsystem

This subsystem was simulated using the optical parameters presented in Table 3, which were based on typical values and experimental data of FSO systems [1, 12, 16, 44]. An operational range was defined for the scenario described in Fig. 1. Thus, the proposed FSO system must meet the length range and changes in atmospheric loss, specified in Table 3. The scintillation loss depends on distance, so it is variable. The divergence angle was made variable to evaluate its influence.

The atmospheric loss range, adopted in this work, was based on the Malaysia KL model [20], which predicts a maximum atmospheric loss of 3 dB/km, for rain rates up to 10 mm/h, in a tropical climate. Besides, data collected in 2020, relating to rainfall rates in Rio de Janeiro, show that the atmospheric attenuation is limited to 3 dB/km in, approximately, 99.8% of the time (rain rates < 10 mm/h) [45]. Hence, a conservative atmospheric loss up to 2 dB/km was adopted as the operational range, to privilege the system availability, as explained later.

Table 3. Parameters of the FSO System

Parameter	Description	Value
P_{TX}	Laser power	14 dBm
L	Link length	3 – 5 km
α_{atm}	Atmospheric loss	$\leq$ 2 dB/km
α_T	Insertion losses in transmitter	1 dB
α_R	Insertion losses in receiver	1 dB
α_{scint}	Scintillation loss	1 – 1.56 dB
d_t	FSO transmitter diameter	5 cm
d_r	FSO receiver diameter	20 cm
θ	Divergence angle	1 – 3.5 mrad
S_r	FSO receiver sensitivity	–36 dBm
λ	Signal wavelength	1550 nm
λ_b	Beacon wavelength	785 nm
R_b	Data bit rate	1 Gbps

On one hand, FSO transceivers operating without an ATP (Acquisition, Tracking, and Pointing) system usually have a divergence angle of 2 to 10 mrad, to compensate for the effects of platform motions. On the other hand, FSO systems that have an ATP mechanism can operate with a narrower divergence angle (0.05 – 1 mrad), thus increasing the system's range [16]. In communications tests between US naval ships, conducted by the NRL, for example, the FSO tranceivers were configured with ATP and θ = 1 mrad [1]. In the present study, we propose the use of a CW laser on another wavelength (see Tab. 3), as a beacon, to signalize if the link is ready to transmit.

The optical subsystem is analyzed in terms of divergence angle, length and atmospheric loss in the following subsections.

B.1. Divergence angle

Initially, the received power was evaluated as a function of total misalignment, for different divergence angles, using L = 3 km and α_{atm} = 1 dB/km. Considering a condition of perfect alignment (d = 0 m), Fig. 7 shows the optical power decreasing, due to the increase in the angle of divergence. This reduction is caused by the increase in geometric loss. We can also see that the power decreases as the total misalignment increases. Besides, higher beam divergences increase the maximum allowed misalignment (d_{max}), making the FSO system less sensitive to the hydrodynamic motions. For example, at 3.5 mrad and 4 mrad, the link is operational for $d \leq$ 6.345 m and 6.792 m, respectively.

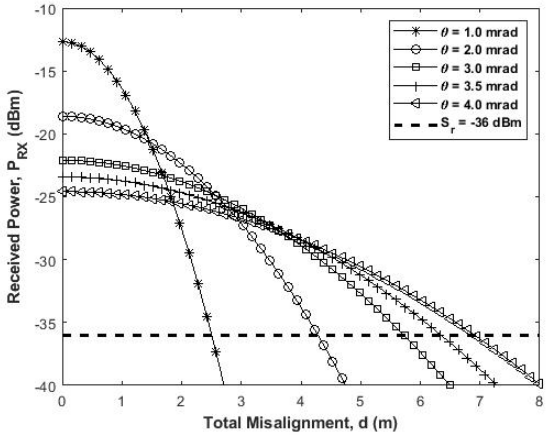

Fig. 7. Received power as a function of total misalignment for different divergence angles (L = 3 km, α_{atm} = 1 dB/km).

Table 4. Maximum Misalignment (d_{max} in meters) for Different Divergence Angles and Atmospheric Losses (L = 3 km)

α_{atm}	θ (mrad)				
(dB/km)	1.0	2.0	3.0	3.5	4.0
1	2.503	4.279	5.758	6.345	6.792
2	2.337	3.894	5.105	5.535	5.888
3	2.123	3.328	4.232	4.533	4.683

Other simulations were carried out for L = 3 km and different values of α_{atm}. Table 4 consolidates these results. As a general behavior, increasing the divergence angle up to 4 mrad, increases d_{max}, while increasing α_{atm} up to 3 dB/km decreases d_{max}.

Fig. 8 shows the results for L = 5 km and α_{atm} = 2 dB/km. In comparison to Fig. 7, the increase of 2 km in L and 1 dB/km in α_{atm} caused a reduction in d_{max} for the entire range of θ. For example, d_{max} was reduced to 2.271 m for θ = 3.5 mrad, while the system becomes inoperative for θ = 4 mrad. Unfortunately, when further increasing α_{atm}, the system only works for very small values of θ, which implies in small values of d_{max} and, consequently, low probability of operating at shaky sea conditions.

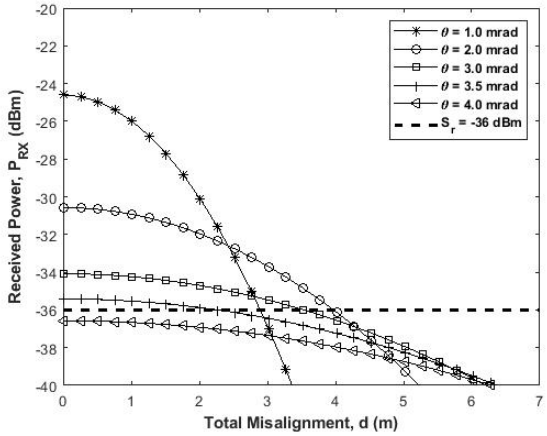

Fig. 8. Received power as a function of total misalignment for different divergence angles (L = 5 km, α_{atm} = 2 dB/km).

In this work, the optimum divergence angle was analyzed in terms of d_{max}. This way, independently if the sea conditions generate high motions, the system was dimensioned with a divergence angle that optimizes the range of possible displacements and, thus, maximizes the link availability. Fig. 9 shows the range of d_{max}, in the form of contour lines, within the operational range, for α_{atm} = 2 dB/km. The blank area at the upper right corner represents the region where no misalignment is possible because it is at the right of the line where d_{max} = 0.0 m. Hence, this Figure also demonstrates that θ = 4 mrad is not a possible angle. This way, we decided to chose θ = 3.5 mrad and to privilege the link availability for L = 3 km (d_{max} = 5.535 m) in detriment of L = 5 km (d_{max} = 2.271 m). Another possible solution could be choosing θ = 2 mrad, where $d_{max} \approx$ 4 m for the entire range of link distances, but this choice would compromise the availability for α_{atm} = 1 dB/km.

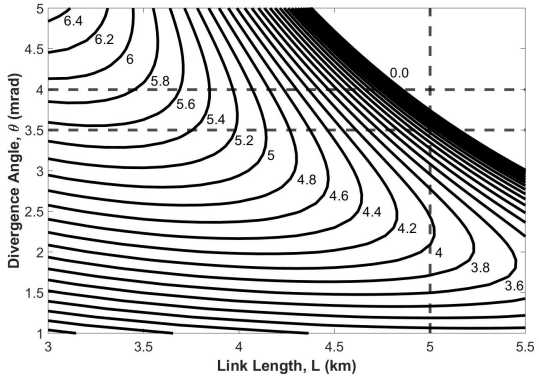

Fig. 9. Contour plot of d_{max} (m) as a function of link length and divergence angle (α_{atm} = 2 dB/km).

The received optical power as a function of time is shown in Fig. 10. It is possible to observe that, for θ = 1 mrad, the power reaches the reception threshold more frequently then for θ = 3.5 mrad. Hence, the availability is higher, remaining above the sensitivity for longer periods, when θ = 3.5 mrad.

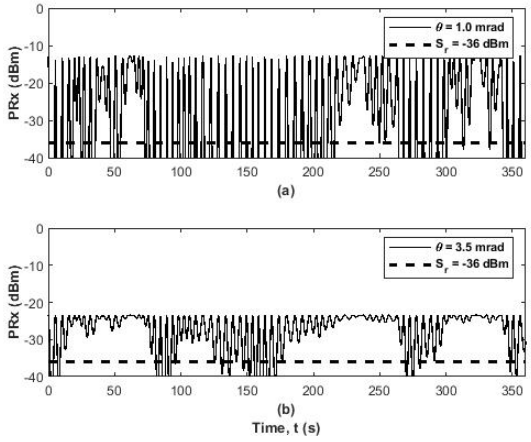

Fig. 10. Received power as a function of time for (a) θ = 1 mrad, and (b) θ = 3.5 mrad. (L = 3 km, α_{atm} = 1 dB/km).

B.2. Link length and atmospheric loss

Subsequently, considering θ = 3.5 mrad, the proposed model was simulated for different distances. Fig. 11 shows these results. For L = 5 km, the optical power drastically reduces, in comparison to 3 km, but remains above the reception threshold. In this case, the FSO system operates with d_{max} = 7.034 m. When $L >$ 7.5 km, we observe that the received optical power remains below the reception threshold and the system becomes inoperative.

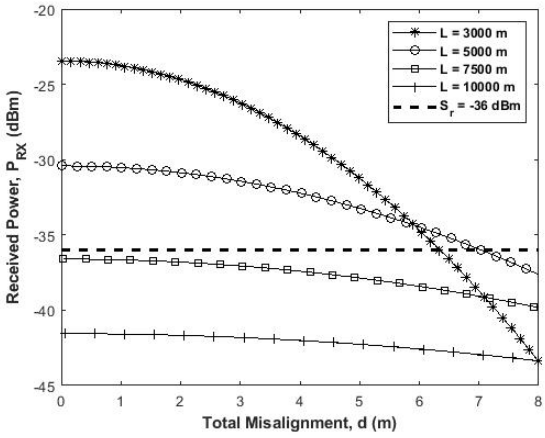

Fig. 11. Received power as a function of total misalignment for different distances (θ = 3.5 mrad, α_{atm} = 1 dB/km).

The same simulations were performed for α_{atm} = 2 and 3 dB/km. The results are presented in Fig. 12. It shows that an increase in L, and the consequent increase in atmospheric and scintillation losses, considerably reduces the received power. In this case, when L = 5 km, despite the reduction of d_{max} to 2.271 m, the FSO system can still operate for α_{atm} = 2 dB/km, but becomes inoperative for α_{atm} = 3 dB/km.

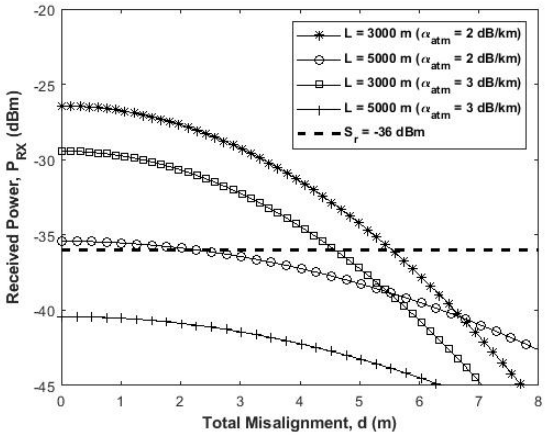

Fig. 12. Received power as a function of total misalignment for different distances (θ = 3.5 mrad, α_{atm} = 2 and 3 dB/km).

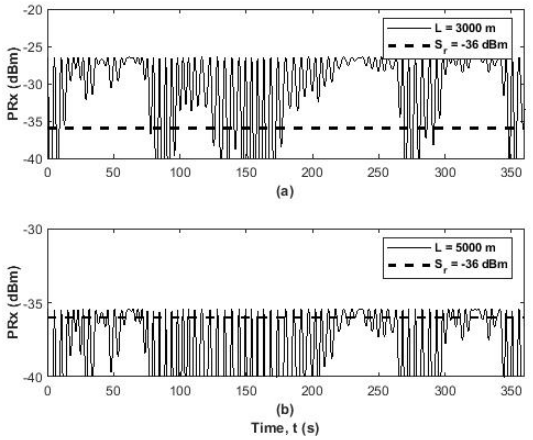

Fig. 13. Received power as a function of time for (a) L = 3 km, and (b) L = 5 km (θ = 3.5 mrad, α_{atm} = 2 dB/km).

These impacts were also perceived during the temporal analysis, shown in Fig. 13. When L = 3 km and 5 km, the FSO receives a maximum P_{RX} of -26.436 dBm and -35.418 dBm, respectively.

Thus, through the analyzes described in this section, it is possible to conclude that a divergence angle of 3.5 mrad was more suitable to compensate for the platform motions, within the predefined operational range: 3 km $\leq$ L $\leq$ 5 km and 1 dB/km $\leq \alpha_{atm} \leq$ 2 dB/km.

C. Availability Analysis

In this subsection, the FSO system is analyzed in terms of availability. The influence of the wave parameters (H_s and T_p) is also considered. As depicted in Subsec. C, the system availability rate was evaluated within the proposed operational range.

C.1. Availability Rates

As previously said, the sea state (H_s = 0.25 m, T_p = 11 s, χ =135°) was chosen to evaluate the impact of a resonant state. Hence, the availability rates for this state are shown in Tab. 5. In this Table, each result was calculated for the following conditions: η_1, for L = 3 km and α_{atm} =1 dB/km; η_2, for L = 3 km and α_{atm} =2 dB/km; η_3, for L = 5 km and α_{atm} =1 dB/km; and η_4, for L = 5 km and α_{atm} =2 dB/km.

Table 5. FSO System Availability (η)

θ (mrad)	η_1 (%)	η_2 (%)	η_3 (%)	η_4 (%)
1.0	43.500	40.813	36.667	29.875
2.0	66.625	61.917	54.938	41.438
3.0	80.000	74.688	63.313	37.125
3.5	84.771	78.979	65.833	22.646
4.0	88.667	81.750	66.542	0.000

For L = 3 km, it is noticed that the availability rates are higher for higher divergence angles. This behavior is also observed in the next two columns. However, when the FSO link reaches 5 km, under the influence of α_{atm} = 2dB/km, the receiver operates so close to its sensitivity that the availability becomes lower, until it reaches zero. Thus, to meet the operating conditions, divergence angles higher than 3.5 mrad are not recommendable.

Table 6. Scatter Diagram of Availability Rates (L = 3 km, θ = 1 mrad)

H_s (m)	T_p (s)							H_{srp} (m)
	2 - 4	4 - 6	6 - 8	8 - 9	10 - 12	12 - 14	14 - 16	
7.5 - 8.0					2.000			7.75
7.0 - 7.5					2.182	2.302		7.25
6.5 - 7.0					2.401	2.537		6.75
6.0 - 6.5				3.141	2.719	2.891		6.25
5.5 - 6.0				3.526	3.136	3.250	4.490	5.75
5.0 - 5.5			3.370	3.880	3.641	3.698	5.047	5.25
4.5 - 5.0			6.250	4.448	4.235	4.313	5.844	4.75
4.0 - 4.5			7.125	5.224	4.938	5.115	6.922	4.25
3.5 - 4.0			8.110	6.005	5.885	6.235	8.255	3.75
3.0 - 3.5		35.167	9.469	7.094	7.068	7.630	9.891	3.25
2.5 - 3.0		41.682	11.422	8.547	8.542	9.531	12.047	2.75
2.0 - 2.5		50.156	14.443	10.688	10.792	12.078	15.047	2.25
1.5 - 2.0	100	61.761	18.787	13.948	14.037	15.839	19.568	1.75
1.0 - 1.5	100	77.255	26.188	19.578	19.417	22.417	26.698	1.25
0.5 - 1.0	100	96.866	42.417	31.584	30.599	33.693	37.938	0.75
0.0 - 0.5	100	100	88.860	69.438	59.849	61.328	65.953	0.25
T_{prp} (s)	3	5	7	9	11	13	15	-

Table 7. Scatter Diagram of Availability Rates (L = 3 km, θ = 3.5 mrad)

H_s (m)	T_p (s)							H_{srp} (m)
	2 - 4	4 - 6	6 - 8	8 - 10	10 - 12	12 - 14	14 - 16	
7.5 - 8.0					7.589			7.75
7.0 - 7.5					8.325	9.151		7.25
6.5 - 7.0					8.907	9.880		6.75
6.0 - 6.5				9.703	9.719	10.844		6.25
5.5 - 6.0				10.604	10.714	11.948	14.896	5.75
5.0 - 5.5			15.855	11.714	11.750	13.219	16.474	5.25
4.5 - 5.0			17.625	13.787	12.943	14.761	18.302	4.75
4.0 - 4.5			19.740	14.579	14.625	16.656	20.427	4.25
3.5 - 4.0			22.250	16.589	16.547	18.870	23.073	3.75
3.0 - 3.5		76.042	25.484	19.110	18.990	21.792	26.130	3.25
2.5 - 3.0		83.354	29.964	22.209	22.266	25.370	30.120	2.75
2.0 - 2.5		88.110	36.073	26.985	26.526	29.969	34.360	2.25
1.5 - 2.0	100	96.391	45.724	33.682	32.637	35.688	39.557	1.75
1.0 - 1.5	100	99.271	60.021	44.526	40.984	43.568	46.122	1.25
0.5 - 1.0	100	100	83.219	63.407	54.943	56.119	60.141	0.75
0.0 - 0.5	100	100	99.719	95.891	91.624	92.391	95.542	0.25
T_{prp} (s)	3	5	7	9	11	13	15	-

Finally, the system availability rates were obtained for each pair of representative values (H_s, T_p), shown in Tab. 1, and for each one of the four wave incidence angles (χ). Thus, at the end of this process, 312 representations of the sea state were used. Tables 6 and 7 show the availability rates, averaged from the four wave incidences, and calculated for L = 3 km, θ = 1 mrad (Tab. 6) and θ = 3.5 mrad (Tab. 7).

C.2. Boresight Error

All results presented in the previous sections were obtained considering the sea motions as the influence of jitter on the pointing error. That is, initially, TX and RX were considered at a condition of link alignment. The impacts caused by the boresight error (δ) in the pointing of the FSO system were inserted as fixed displacements in the horizontal ($x_c + \delta$) and vertical ($y_c + \delta$) components of Eq. 6. Thus, an evaluation of the availability rate was made, for the sea state (H_s = 0.25 m, T_p = 11 s, χ =135°) and different values of δ, obtaining the results presented in Fig. 14.

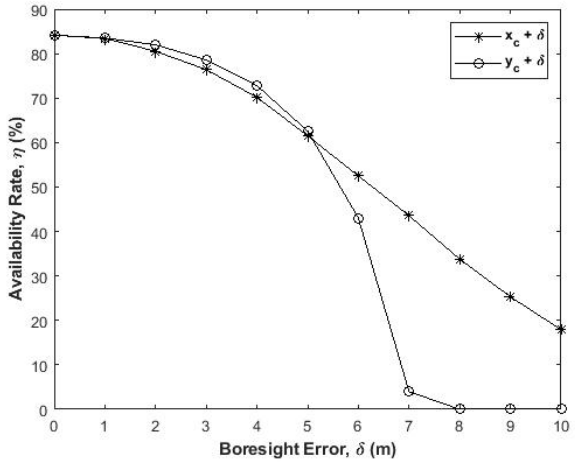

Fig. 14. Boresight Error Analysis (H_s = 0.25 m, T_p = 11 s, χ = 135°, L = 3 km, θ = 3.5 mrad, α_{atm} = 1 dB/km).

The curves in Fig. 14 show that, when $\delta = 0$, the availability rate is equal to 84.771%, the same result shown in Tab. 5. With increasing boresight errors, there is a continuous reduction in the system availability, due to the increase in the values of δ. When δ = 5 m, the difference between the two availabilities is quite small: 61.5%, for the horizontal boresight error, and 62.58%, for the vertical one. However, for δ = 6 m, the boresight error starts to significantly influence the misalignment on the y axis, so that when δ = 7 m, there is an abrupt drop in the system availability rate (3.98%) and, when δ = 8 m, the link becomes inoperative. On the other hand, when δ = 10 m on the horizontal boresight error, the system operates with low availability (17.92%).

This abrupt drop in performance caused by the increase in boresight error on the vertical axis is due to impacts caused by the resonance peak of the pitch movement observed at $T_p = 11s$. For this same T_p, it is observed that the resonance peak of the yaw rotation is lower, making the boresight error less impactful on the horizontal axis compared to the vertical axis. In addition, an error of δ = 6 m is very near the maximum displacement observed for this configuration in Tab. 4 (d_{max} = 6.345 m).

C.3. Significant Wave Height

Fig.15 shows the availability of the system as a function of H_s. The results were obtained by averaging each line in Tables 6 and 7. As expected, it can be seen that the availability decreases due to the increase in wave heights. Furthermore, the curves show that this reduction occurs in a similar way for the two systems, being the availability higher for θ = 3.5 mrad.

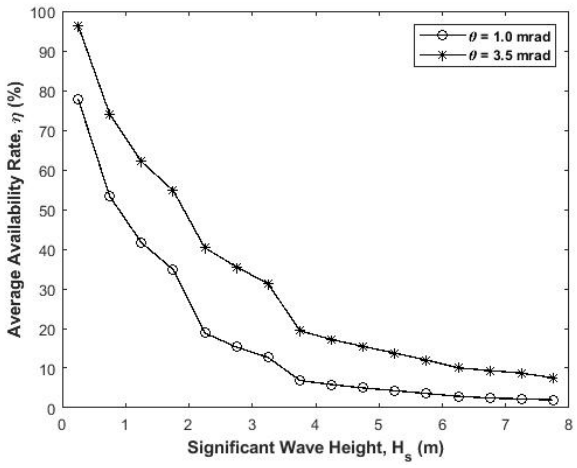

Fig. 15. Average availability as a function of significant wave height.

C.4. Peak Period

Similar to the analysis made for H_s, the average availability as a function of peak period (T_p) was calculated and its values were represented in Fig. 16.

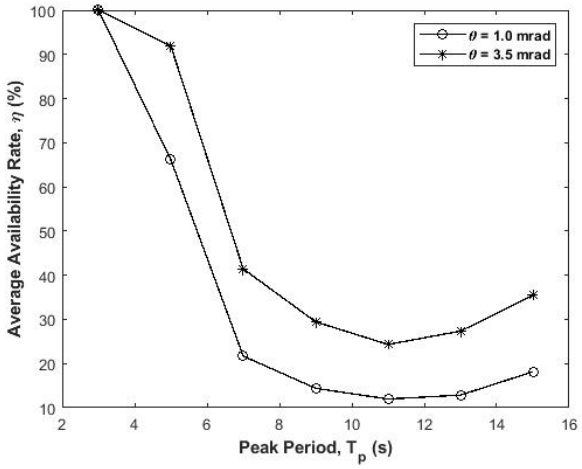

Fig. 16. Average availability in function of the peak period.

The curves show a similar behavior, regarding the analyzed peak periods. For both values of θ, the availability rates decrease rapidly, up to T_p = 11 s when they start to slightly increase again. In this case, it is possible to conclude that the variations in the availability rates, observed in Fig. 16, follow the hydrodynamic behavior of the vessel. This happens especially in the presence of motions that create resonating frequencies, such as those described by the pitch and yaw RAO curves, for $\chi = 135°$ (see Fig. 5 (e) and (f)). Therefore, the availability of the FSO system on board the Mariner can be described by the RAO curves that most affect the stability of the maritime platform.

C.5. Expected Data Rates

As previously said, the proposed system posses a beacon laser, on another wavelength, which signalizes if the link is ready to transmit. This way, it is capable of detecting the uptime windows, such as those presented in Figs. 10 and 13, and immediately transmit data at full rate. Hence, considering that the communication link has a bit rate of 1 Gbps, due to the succession of up and downtime windows of availability, in a long time, the link presents an effective data rate, given by the availability rate multiplied by the bit rate.

In order to know which data rate to expect in such random conditions as the sea, the availability rates of Tables 6 and 7 were divided in ranges of 5% and the probability of occurrence of each range was calculated based on Tab. 1. Fig. 17 shows the cumulative probability of occurrence for each availability rate range. The availability rate axis was purposely inverted to show the probability of high data rates first.

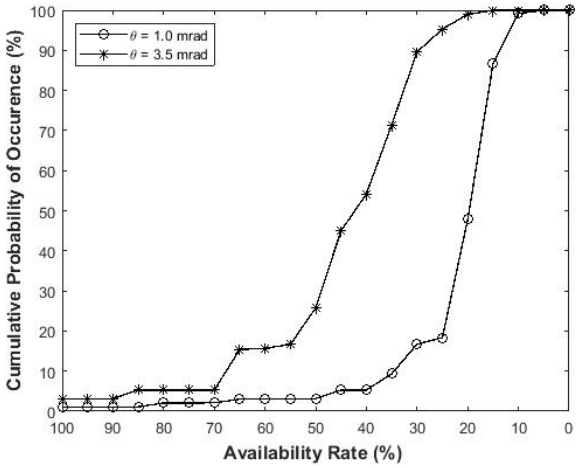

Fig. 17. Cumulative Probability of Occurrence in function of Availability Rate Ranges.

The curves show that the system has a low probability of operating with an availability above 70% (5.3%, for 3.5 mrad, and 2.1%, for 1 mrad). This availability corresponds to an effective data rate of 700 Mbps. Later, it is observed that the probability of the system to operate above 500 Mbps increases to 25.8%, for 3.5 mrad, but it remains practically unchanged (3.2%) for 1 mrad. Finally, with 90% of confidence, the system operates at an effective rate of 300 Mbps and 136,6 Mbps, for each one of the analysed divergence angles.

4. CONCLUSION

In this work, the availability of an FSO communication link, established between a maritime platform and a land base, was analyzed. To achieve this goal, the hydrodynamic system was modeled to determine the most appropriate angle of divergence (3.5 mrad) to compensate for geometric and misalignment losses in given operational conditions.

Despite the dependence of hull geometry and sea conditions, the presented methodology is applicable to any maritime platform. Thus, it was demonstrated that, for the considered FSO and vessel alignment, pitch and yaw rotations have a great impact on the misalignment of the link. An analysis based on RAO curves was done and it showed its relation to the behavior of the communication system. The use of Marcum's Q function is suitable for this kind of application, which involves several sea states, as it is rapidly processed.

The optical subsystem was analyzed in terms of divergence angle, link length, and atmospheric attenuation. Through this analyzes, it was possible to conclude that a divergence angle of 3.5 mrad was more suitable to compensate for the platform motions, within the predefined operational lengths: 3 km to 5 km. The proposed FSO system was designed to operate under conditions of clean weather and fine fog. This corresponds to an operational range of α_{atm} between 1 dB/km and 2 dB/km. Nevertheless, the system can still work for higher values of α_{atm}, such as 3 dB/km, if the ship's distance to the coast is near 3 km.

In addition, the FSO system availability was analyzed in terms of boresight error, significant wave height, and peak period of the sea spectrum. It was noted that boresight errors above 5 m can reduce drastically the system performance, especially for the vertical axis. Regarding the sea conditions, it is possible to conclude that the availability decreases due to the increase in wave heights or in the presence of motions that create resonating states on the vessel.

The operation at an effective data rate of 300 Mbps, in 90% of the observed sea conditions, was demonstrated, when using a beacon system as PAT. Higher data rates, such as 400 Mbps, are also possible, although less probable ($\leq 50\%$). Therefore, the methodology developed in this article can be used to optimize the availability of FSO links implemented on offshore platforms under the influence of ocean wave motions. In another perspective, this methodology can also be applied to reduce costs in measuring the motions of hydrodynamic systems in a controlled environment.

REFERENCES

1. W. S. Rabinovich, C. I. Moore, R. Mahon *et al.*, "Free-space optical communications research and demonstrations at the US Naval Research Laboratory," Appl. Opt. **54**, F189 (2015).
2. V. G. A. Carneiro, G. K. Rodrigues, and M. T. M. Rocco Giraldi, "Simulation of a temporal hard-limited OCDMA system over FSO link under average turbulence," J. Microwaves, Optoelectronics Electromagn. Appl. **12**, 79–95 (2013).
3. M. A. Khalighi and M. Uysal, "Survey on free space optical communication: A communication theory perspective," IEEE Commun. Surv. Tutorials **16**, 2231–2258 (2014).
4. H. Kaushal, V. Jain, and S. Kar, *Free Space Optical Communication*, Optical Networks (Springer India, New Delhi, 2017).
5. G. K. Rodrigues, V. G. A. Carneiro, A. R. da Cruz, and M. T. M. Giraldi, "Evaluation of the strong turbulence impact over free-space optical links," Opt. Commun. **305**, 42–47 (2013).
6. W. S. Rabinovich, C. I. Moore, H. R. Burris *et al.*, "Free space optical communications research at the U.S. Naval Research Laboratory," in *Free-Space Laser Communication Technologies XXII*, vol. 7587 (2010), p. 758702.
7. H. Kaushal and G. Kaddoum, "Applications of Lasers for Tactical Military Operations," IEEE Access **5**, 20736–20753 (2017).
8. S. Fathi-Kazerooni, Y. Kaymak, R. Rojas-Cessa *et al.*, "Optimal Positioning of Ground Base Stations in Free-Space Optical Communications for High-Speed Trains," IEEE Transactions on Intell. Transp. Syst. **19**, 1940–1949 (2018).
9. X. Chen, J. Ding, H. Lai, S. Fathi-Kazerooni *et al.*, "Performance Analysis of Free Space Optical Communication Systems for High-Speed Trains," IET Optoelectronics **1447**, 1–6 (2019).
10. Q. Fan, M. Taheri, N. Ansari, J. Feng *et al.*, "Reducing the Impact of Handovers in Ground-to-Train Free Space Optical Communications," IEEE Transactions on Veh. Technol. **67**, 1292–1301 (2018).

11. H. S. Khallaf and M. Uysal, "UAV-Based FSO Communications for High Speed Train Backhauling," IEEE Wirel. Commun. Netw. Conf. WCNC **2019-April**, 1–6 (2019).
12. Y. Kaymak, R. Rojas-Cessa, J. Feng, N. Ansari, M. Zhou, and T. Zhang, "A Survey on Acquisition, Tracking, and Pointing Mechanisms for Mobile Free-Space Optical Communications," IEEE Commun. Surv. Tutorials **20**, 1104–1123 (2018).
13. J. C. Juarez, A. Dwivedi, A. R. Hammons, S. D. Jones, V. Weerackody, and R. A. Nichols, "Free-Space Optical Communications for Next-generation Military Networks," IEEE Commun. Mag. **44**, 46–51 (2006).
14. F. Yang, J. Cheng, and T. A. Tsiftsis, "Free-space optical communication with nonzero boresight pointing errors," IEEE Transactions on Commun. **62**, 713–725 (2014).
15. M. Chen, "Robust tracking control for self-balancing mobile robots using disturbance observer," IEEE/CAA J. Autom. Sinica **4**, 458–465 (2017).
16. S. Bloom, E. Korevaar, and J. Schuster, "Understanding the performance of free-space optics [Invited]," J. Opt. Netw. (2003).
17. I. I. Kim and E. J. Korevaar, "Availability of free-space optics (FSO) and hybrid FSO/RF systems," in *Optical Wireless Communications IV,* vol. 4530 E. J. Korevaar, ed., International Society for Optics and Photonics (SPIE, 2001), pp. 84 – 95.
18. A. Prokes, "Atmospheric effects on availability of free space optics systems," Opt. Eng. **48**, 1 – 10 (2009).
19. J. Turán and Ľuboš Ovseník, "Experimental FSO network availability estimation using interactive fog condition monitoring," (SPIE, 2016), pp. 515 – 530.
20. A. A. Basahel, M. R. Islam *et al.*, "Availability assessment of free-space-optics links with rain data from tropical climates," J. Light. Technol. **35**, 4282–4288 (2017).
21. V. V. Mai and H. Kim, "Link availability of airborne free-space optical communication systems under effect of generalized misalignment," in *2018 23rd Opto-Electronics and Communications Conference (OECC),* (2018), pp. 1–2.
22. S. Chandrasekaran, *Dynamic Analysis and Design of Offshore Structures* (Springer Nature Singapore Pte Ltd, Chennai, India, 2018), 2nd ed.
23. Y. Bai and W. L. Jin, *Marine Structural Design* (Elsevier Ltd, Walthan, 2016), 2nd ed.
24. W. Journée, J.M.J., Massie, *Offshore Hydromechanics* (Delft University of Technology, 2001), 1st ed.
25. National Maritime Research Institute (NRMI), "Global Winds and Waves," (2006). Https://www.nmri.go.jp/study/Intellectual/globus/11/32-ann10yrs-hp_e.html, accessed on 19/01/2021.
26. K. Hasselmann, T. Barnett, E. Bouws *et al.*, "Measurements of wind-wave growth and swell decay during the Joint North Sea Wave Project (JONSWAP)," Deutsches Hydrogr. Inst. (1973).
27. L. Roncetti, F. N. Corrêa, C. H. Albrecht, and B. P. Jacob, "Development of Operational Limit Diagrams for Offshore Lifting Procedures," (2015).
28. B. P. Jacob, R. de Almeida Bahiense, F. N. Correa, and B. M. Jacovazzo, "Parallel implementations of coupled formulations for the analysis of floating production systems, part i: Coupling formulations," Ocean. Eng. **55**, 206–218 (2012).
29. R. B. Zubaly, *Applied Naval Artchitecture* (Schiffer Publishing, Ltd, 2015).
30. W. Meyers, D. Sheridan, and N. Salvesen, "Manual – NSRDC Ship-Motion and Sea-Load Computer Program," (1975).
31. C. A. R. Castillo, "Sobre a dinâmica não linear do balanço paramétrico," Ph.D. thesis, Universidade Federal do Rio de Janeiro (2009).
32. N. Salvesen, E. Tuck, and O. Faltinsen, "Ship motions and sea loads," Transactions SNAME **78**, 250–287 (1970).
33. S. D. Manley and J. W. J. Pierson, "On the Motions of Ships in Confused Seas," The Soc. Nav. Archit. Marit. Eng. **61**, 81 (1953).
34. P. Brodtkorb, P. Johannesson, G. Lindgren, I. Rychlik, J. Rydén, and E. Sjö, "WAFO - a Matlab toolbox for the analysis of random waves and loads," in *Proc. 10'th Int. Offshore and Polar Eng. Conf., ISOPE, Seattle, USA,* vol. 3 (2000), pp. 343–350.
35. A. Siegman, "Unstable optical resonators for laser applications," Proc. IEEE **53**, 277–287 (1965).
36. H. Kogelnik and T. Li, "Laser beams and resonators," Appl. Opt. **5**, 1550–1567 (1966).
37. T. S. Khwaja and S. A. Reza, "Low-cost Gaussian beam profiling with circular irises and apertures," Appl. Opt. **58**, 1048 (2019).
38. C. P. Azzolin, A. F. Gurgel, and V. G. A. Carneiro, "Marcum Q-function as an analytical solution for misaligned Gaussian beams," Opt. Eng. **60**, 1 – 10 (2021).
39. L. C. Andrews, R. L. Phillips, C. Y. Hopen, and M. A. Al-Habash, "Theory of optical scintillation," J. Opt. Soc. Am. A **16**, 1417–1429 (1999).
40. L. Dordová and O. Wilfert, "Calculation and Comparison of Turbulence Attenuation by Different Methods," Radioengineering **19**, 162–167 (2010).
41. J. A. H. Osorio, "Simulação e desenvolvimento de um enlace de free-space optics no Rio de Janeiro e a relação com a ITU-T G.826," Ph.D. thesis, Pontifícia Universidade Católica do Rio de Janeiro (PUC-RJ), Rio de Janeiro, Brazil (2005).
42. I. I. Kim, R. Stieger, J. Koontz, C. Moursund, M. Barclay, P. Adhikari, J. J. Schuster, and K, "Wireless optical transmission of fast ethernet, FDDI, ATM, and ESCON protocol data using the TerraLink laser communication system," Opt. Eng. **37**, 3143–3155 (1998).
43. V. G. A. Carneiro, G. K. Rodrigues, and M. T. M. R. Giraldi, "Performance analysis of a 2D double hard-limited OCDMA system over FSO link under strong turbulence for defense applications," in *MILCOM 2012 - 2012 IEEE Military Communications Conference,* (IEEE, 2012), pp. 1–6.
44. A. Touati, A. Abdaoui, F. Touati, M. Uysal, and A. Bouallegue, "On the Effects of Combined Atmospheric Fading and Misalignment on the Hybrid FSO/RF Transmission," Ph.D. thesis (2016).
45. Instituto Nacional de Meteorologia (INMET), "Meteorological database," (2021). Https://bdmep.inmet.gov.br/, accessed on 24/12/2021.